Experimental and Numerical Analysis of Energy Absorption in 3D-Printed Auxetic and Combined Lattice Structures Under Quasi-Static Loading

Hadi Safi Valilu[1], Mohammad Ali Saeimi Sadigh[1*] , Moosa Sajed[1], Vahid Tavousi[2]

[1] Department of Mechanical Engineering, Azarbaijan Shahid Madani University, Tabriz, Iran
[2] Faculty of Mechanical Engineering, K.N. Toosi University of Technology, Tehran, Iran

ARTICLE INFO

Article Type
Original Research

ABSTRACT

This study presents an experimental and numerical analysis of the energy absorption (EA) performance of four types of 3D-printed polylactic acid (PLA) lattice structures under quasi-static compression. The structures included two uniform designs honeycomb (Sample 1) and re-entrant (Sample 2) and two hybrid designs (Samples 3 and 4) combining these unit cells. Experimental testing and finite element simulation revealed that the hybrid designs significantly outperformed their uniform counterparts. Between the cases, sample 4 achieved the highest specific energy absorption (SEA) of 2.41 kJ/kg, surpassing Sample 1 (1.51 kJ/kg) by 62% and Sample 2 (1.65 kJ/kg) by 33%. It also exhibited the highest total EA of 120.15 J and a mean crushing force (MCF) of 5982.96 N. Sample 3 followed closely with an SEA of 2.24 kJ/kg. Finite element analysis showed strong correlation with experimental data, with differences in SEA values across all samples ranging from 9.36% to 16.67%. The results conclusively demonstrate that strategic geometric hybridization of unit cells is a highly effective method for enhancing EA metrics in lightweight structures.

How to cite this article
Safi Valilu H, Saeimi Sadigh M.A , Sajed M, Tavousi V, Experimental and Numerical Analysis of Energy Absorption in 3D-Printed Auxetic and Combined Lattice Structures Under Quasi-Static Loading. Modares Mechanical Engineering; Eng. *2025;25(09):555-565.*

*Corresponding author's email: saeimi.sadigh@azaruniv.ac.ir
*Corresponding ORCID ID: *0000-0001-8500-4083*

1- Introduction

As time progresses and science advances and aligns with industry, there arises a need to develop and enhance materials with new and different characteristics that differ from the existing conventional ones [1, 2]. Metamaterials are artificial materials that possess unique characteristics that go beyond the properties of conventional materials. These characteristics arise from their geometric structure, meaning the chemical composition of these structures has no role in these characteristics [3-5]. One of the most well-known metamaterials are auxetic materials, which exhibit completely different behavior in deformation compared to conventional materials. Conventional structures used in industry, when subjected to tension, increase in length in the direction of the applied stress and contract laterally. These types of materials have a positive Poisson's ratio. However, unlike these materials, auxetic materials, when subjected to tension, expand laterally, and when subjected to compression, contract laterally. These materials have a negative Poisson's ratio [6-9]. These auxetic structures, which have a negative Poisson's ratio, possess remarkable mechanical properties. Among these characteristics are indentation resistance [10], shear resistance [11], fracture resistance [12], fracture toughness, and EA [2, 13, 14].

Cellular structures have attracted significant attention due to their light weight and good mechanical properties, as well as the mentioned characteristics. Today, with research and innovation in the type of structure and cell geometry of these structures, new samples are introduced and compared and analyzed against existing structures [15]. One of the most important unique features of auxetic structures is their high EA per unit mass, known as SEA. Furthermore, various studies are conducted on high EA with less mass of the structure [14, 16]. These structures, which have a high SEA, are widely used in various industries such as aerospace, medicine, automotive, and engineering structures [17]. In sandwich structures, which are made from two plates and a low-density core, these materials can be used as the core due to their lower weight, high stiffness, and EA. Also, well-known structures such as honeycomb structures can be used as the core [18, 19]. The most important feature for EA from these structures is the geometric design of the cell. Famous geometric structures include honeycomb, re-entrant, tetrachiral, and antitetrachiral. In other cases, combining unit cells of these structures in different ways can lead to more desirable results [20-24]. Additive manufacturing, in general, is known as rapid prototyping or layer-by-layer production. Today, using 3D printing technology, various complex parts can be produced, which are used in various industries. 3D printing technology is used as an equivalent to additive manufacturing [25]. 3D printing is one of the methods for producing auxetic structures because, as mentioned, this method is suitable for creating various complex structures. This method is one of the popular options due to its precise material fabrication, cost-effectiveness, and suitable production time for auxetic structures [26-28]. For the input material of these structures, thermoplastic polymer materials are usually used.

In one of the recent studies, Shokri Rad et al. [29] focused on determining EA from auxetic structures. In their study, they examined the impact of single cell configuration of various structures on EA under quasi-static and dynamic loads. They observed that auxetic structures, due to their ability to withstand quasi-static axial impact loads, have superior impact resistance and EA compared to nonauxetic structures. They also presented a numerical study on their proposed structures.

Among the studies conducted in these fields, Yusefi et al. [30] introduced three-dimensional structures that use both soft and hard polymers for EA. They modelled their designs after snowflakes and produced them from thermoplastic polyurethane (TPU) and polyamide 12 (PA 12). To determine and compare the EA capabilities of the structures, they performed compression tests. They also employed the finite element method and compared the numerical results with experimental data. Their findings showed that TPU auxetics exhibit stress softening, hysteresis, cyclic stress softening, and high energy absorption/dissipation, whereas PA 12 demonstrated elastoplastic behaviors with some residual strains and superior energy absorption/dissipation performance. Also in some studies, to enhance mechanical properties and increase EA capacity, straight blades or sinusoidal-shaped blades were added to the unit cells of the re-entrant structure, resulting in a different structure [31-34].

In another study, Zahed et al. [35] focused on reinforcing re-entrant structures. They modified the geometry of the unit cell and designed six new structures by adding additional struts as supports to enhance the SEA capacity and flexural modulus. The results showed that adding supports significantly increases the maximum force tolerated by the structure at the same displacement compared to traditional re-entrant structures. Additionally, the findings indicate that honeycombs with concave curved supports outperform conventional re-entrant honeycombs, improving the flexural modulus (Ef) by approximately 282% and enhancing EA and SEA by over 297%. Furthermore, angle support structures demonstrate outstanding outcomes compared to simple straight supports and single-support structures. Wang et al. [36] also studied a new auxetic honeycomb called re-entrant star-shaped honeycomb (RSH) and analyzed its in-plane impact responses both theoretically and numerically. They observed three types of microstructural deformation modes under different impact velocities: low-velocity mode, medium-velocity mode, and high-velocity mode. Additionally, a deformation map was summarized to illustrate the effects of impact velocity and relative density on the deformation modes. As mentioned, one of the methods for constructing these structures is to combine them. To this end, Ebrahimi et al. [37] produced four new hybrid metamaterial structures by combining honeycomb, re-entrant, and star-shaped unit cells using additive manufacturing (AM) techniques and then tested them to evaluate the improved mechanical properties. They compared the in-plane EA capacity and uniaxial compressive response of these new structures using finite element simulations and experimental techniques. They concluded that the re-entrant-star-shaped (RS1) structure exhibited higher compressive strength, plateau stress, and EA than the other structures, primarily due to its unique deformation mechanism. For comparing the EA and mechanical properties between the original cellular and hybrid structures (HCS), RS1 had the best performance. Additionally, the Poisson's ratio curve for HCS was obtained and the relevant results were analyzed. Alomarah et al. [38] A re–entrant chiral auxetic structure (RCA) is a recently developed structure, which combines the topological features of re–entrant and chiral honeycombs. Comparative study between the RCA structure and popular benchmarks subjected to uniaxial compression has been conducted experimentally and numerically. The samples were fabricated from polyamide 12 (PA12) using the Multi Jet Fusion (MJF) process. The experimental results showed that the high accuracy of the MJF process to produce robust components with precise details. It has been found that the RCA structure outperforms the other types of honeycombs in terms of strength and SEA when loaded in the Y direction, while only the tetrachiral honeycomb surpasses the RCA structure in terms of SEA when loaded in the X direction. The auxeticity (NPR) of the RCA structure compressed in the Y direction was larger than that of the other honeycombs. In other study, Johnston et al. [39] explored the use of multiple materials in three well-known cellular geometries and compared their performance. They introduced two types of auxetic structures (Re-entrant and anti-tetrachiral) and one type of non-auxetic structure (hexagonal honeycomb). For each geometry, three different material configurations were used: a single-material structure with PLA, and two multi-material structures: PLA-Nylon and PLA-Thermoplastic Polyurethane (TPU). The results showed that in cases where single loading cycles are required, single-material structures perform best and absorb the most energy. However, for multiple loading cycles, multi-material structures offer the best solution because compression

occurs through elastic buckling instead of plastic buckling in single-materials. Additionally, it was found that by introducing materials with different stiffness in specific areas of the structure, the Poisson's ratio during compression can be altered for Re-entrant and honeycomb geometries.

In another study, Yuan et al. [40] proposed the creation of three-dimensional metamaterials from auxetic composite networks through laser sintering of CNT-reinforced nanocomposites, providing a platform for designing and manufacturing systems with programmable EA capabilities. Optimization of the constituent materials and structural design enables improved EA performance at various scales. Their study results showed that the EA capacity of auxetic metamaterials increases exponentially with a relative density of approximately 2.5 ~ 3. Auxetic metamaterials with a reasonable topology demonstrated a combination of high specific compression resistance (0.0195 MPa per kg/m³), exceptionally high EA capacity (6.29 MJ/m³), and excellent SEA (20.42 J/g).

Wu et al. [41] presented a fractal-like tree method for developing a novel protective structure with high EA capability in their study. These structures are designed with fractal tree-like shapes such as triangular, square, and pentagonal, and their mechanical behaviors and deformation processes are examined through quasi-static axial compression tests. Najafi et al. [42] also examined the ability of some well-known auxetic structures to absorb energy under low-velocity and quasi-static transverse loading. They produced samples with three types of geometry (re-entrant, arrowhead, and anti-tetra chiral) using additive manufacturing (3D printing) and compared the EA and failure mechanisms of all three structures under both types of loading. In general, extensive studies have been conducted on cellular structures due to their wide range of applications, which include energy absorbing structures, thermal insulators, sound dampers, and scaffolds for medical engineering [43-48].

In recent studies conducted by Sarkhosh [49] a novel honeycomb structure with enhanced SEA was introduced, featuring internal cell walls reinforced with a hexagonal spiral pattern. The effect of filling the void spaces between the cells with rigid polyurethane foam under quasi-static loading conditions was also investigated. The spiral-reinforced design, combined with foam filling, significantly improved EA performance and presents a promising alternative to traditional honeycomb structures in the core of energy-absorbing sandwich panels. Also, in Another study [50, 51] introduced a gradient

honeycomb structure inspired by sunflowers, in which the hexagonal cells gradually decrease in size along the radius. The aim was to overcome the load-bearing limitations of traditional honeycomb designs. The results showed significant improvements in EA, SEA, and crushing force efficiency (CFE) compared to conventional structures—up to 14% in EA, 27% in SEA, and 45% in CFE. These enhancements highlight the strong potential of this innovative structure as an effective energy absorber in sandwich panels, aircraft components, and automotive bumpers.

This study advances the field of energy-absorbing metamaterials by systematically investigating how the strategic integration of auxetic and conventional lattice geometries enhances mechanical performance. In contrast to prior research, which has predominantly focused on uniform auxetic structures or multi-material composites, this work introduces a novel design paradigm based on the geometric hybridization of unit cells within a single material system. Unlike existing studies that modify individual cell configurations or employ complex material compositions, we demonstrate that an intelligent combination of cell types in monolithic PLA structures can achieve superior SEA without increasing material complexity. The findings provide new insights into leveraging geometric arrangement, in addition to material composition, to optimize EA. This approach offers significant practical advantages for applications requiring lightweight, single-material solutions.

2- Materials and Methods
2-1- Geometry of Structures
This study aims to enhance EA and SEA through the strategic combination of auxetic and conventional lattice structures. A comparative analysis was conducted to evaluate the performance of uniform lattices against their hybrid counterparts. Four distinct structures were designed with constant overall dimensions (45×45×45 mm) to ensure a valid comparison: (1) a uniform conventional honeycomb; (2) a uniform re-entrant auxetic structure; (3) a hybrid structure integrating the re-entrant and honeycomb unit cells; and (4) a second-order hybrid structure combining the first hybrid with the uniform re-entrant lattice. All unit cell geometries were maintained at a consistent scale across the samples. Figure 1 illustrates the unit cell dimensions and overall sample geometry, while Figure 2 presents the complete computer-aided design (CAD) models generated in SolidWorks.
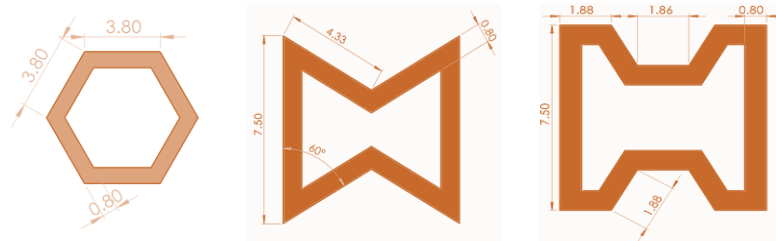

Fig.1 Unit cells of the samples

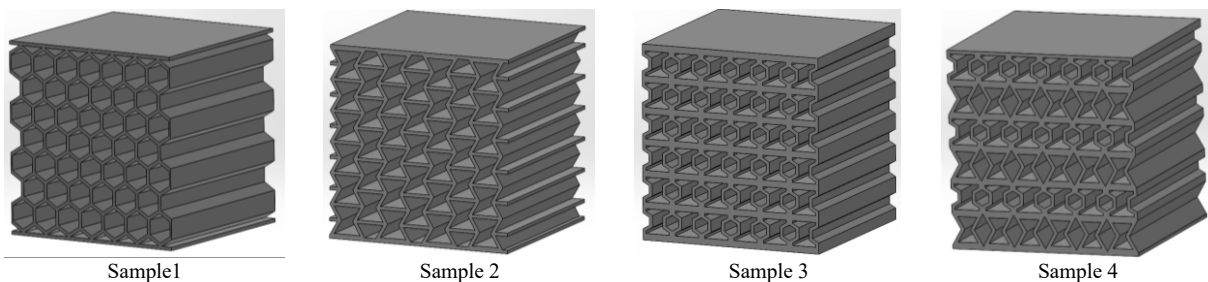| Sample1 | Sample 2 | Sample 3 | Sample 4 |

Fig.2 General view of the samples

This study evaluates the SEA of four distinct lattice structures. The primary objective is to compare the performance of the hybrid designs (Samples 3 and 4) against the uniform baseline structures (Samples 1 and 2). All samples were fabricated PLA using additive manufacturing. Mechanical performance was assessed through experimental uniaxial compression tests, the results of which were validated against simulations conducted via finite element analysis (FEA).

2-2- Sample Fabrication

The structures were constructed using a 3D printer (3DPE) made by Tosegaran Boed Sevvom, based on Fused Deposition Modelling (FDM). Lattice structures were designed in SolidWorks and exported in STL format for processing in Simplify3D, where they were converted into G-code. A consistent set of printing parameters, including layer thickness, print angle, and print speed (detailed in Table 1), was maintained for all samples to ensure comparability. To mitigate first-layer adhesion issues, a three-layer support structure was printed beneath each specimen and subsequently removed post-fabrication. A view of the 3D printing system is provided in Figure 3. The final printed specimens, prepared for compressive testing, are shown in Figure 4.

Table.1 Parameters of 3D printing structures

Samples print speed	Layer thickness	Layer print angle	Nozzle temperature	Bed temperature	Filament diameter	Nozzle diameter
4000 mm/min	0.2 mm	±45	210 ºC	0 ºC	1.75 mm	0.2 mm

Fig.3 3D printing system

Sample 1	Sample 2	Sample 3	Sample 4
Mass= 30.05 gr Volume=24240 mm³	Mass= 36.30 gr Volume=29278 mm³	Mass= 53.12 gr Volume=42845 mm³	Mass= 48.87 gr Volume=39413 mm³

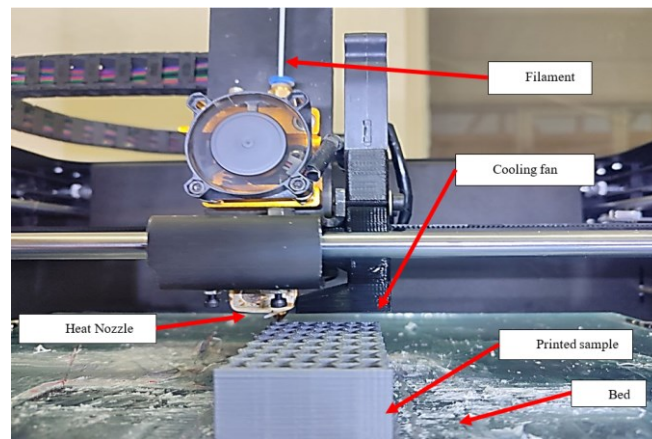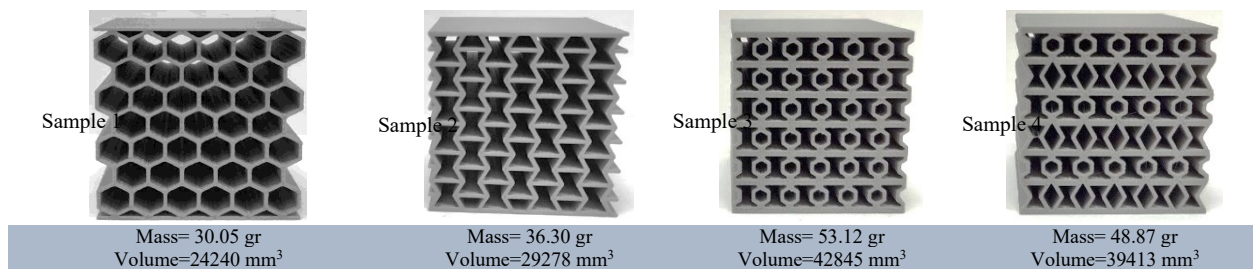**Fig.4** printed samples and their mass and volume properties

2-3- Evaluation Criteria

After completing the simulation and obtaining the results, the optimal structure among the four structures must be identified. To evaluate the crushability of the structures, three key indicators were used: EA, SEA, Mean Crushing Force (MCF) and Peak Crushing Force (PCF). To assess the total EA, which is the amount of strain energy, the following equation is used:

$$EA = \int_0^d f(x)d_x \tag{1}$$

where $f(x)$ is the crushing force and d is the displacement during the crushing phase. Among these indicators, the most important is SEA, which represents the energy absorbed per unit mass. It is defined as:

$$SEA = \frac{EA}{m} = \frac{\int_0^d f(x)d_x}{m} \tag{2}$$

where m is the mass of the lattice structures. The MCF indicator, used for a specified deformation, is expressed as:

$$MCF = \frac{EA}{d} = \frac{\int_0^d f(x)d_x}{d} \tag{3}$$

Additionally, the parameter defining the crushing force efficiency (CFE) is a critical feature for comparing and assessing energy-absorbing structures through crushing, expressed by Formula (4):

$$CFE = \frac{MCF}{PCF} \tag{4}$$

Experimental Tests

3-1- Tensile test

To characterize the mechanical properties of the PLA material for finite element modeling (FEM), standard tensile specimen was fabricated in accordance with ASTM D638. The specimens were produced using the printing parameters detailed in the previous section. Quasi-static uniaxial tensile tests were conducted on a universal testing machine at a constant crosshead displacement rate of 3 mm/min. The resulting stress-strain data were used to extract the essential material properties. Figure 5 depicts the ASTM D638 specimen geometry, the manufactured samples, the testing apparatus, and a representative stress-strain curve. The resultant material properties are summarized in Table 2.
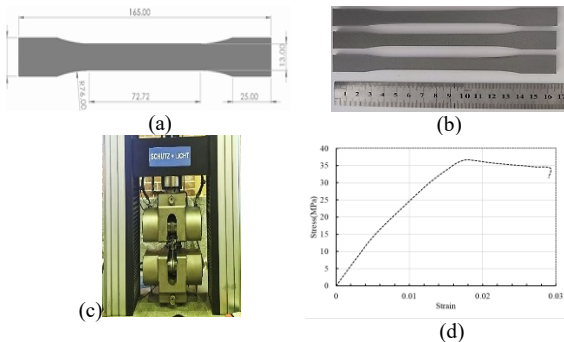
Fig.5 (a): Standard tensile test sample (b): produced samples (c): tensile testing machine (d): and stress-strain curve.

Table.2 Material properties

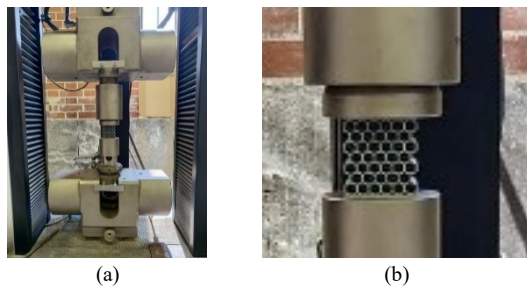| Elastic Modulus (MPa)	Yield Strength (MPa)	Ultimate Strength (MPa)
2073	33.93	36.67

Fig.6 Compression test equipment (a): testing machine (b): specimen placement.

3-2- Compression test

Quasi-static uniaxial compression tests were performed on the fabricated lattice specimens using a SCHÜTZ-LICHT universal testing machine. Tests were conducted at a constant crosshead displacement rate of 3 mm/min. Force-displacement data were recorded for subsequent analysis. The compression process was recorded using a digital camera to facilitate a qualitative comparison of deformation modes with subsequent FEA. The experimental setup, including the testing machine and a specimen under compression, is shown in Figure 6.

4- Finite Element Method

In this study, the Abaqus software was used for simulation. Initially, the designed CAD files were imported into Abaqus. Then, as mentioned in the previous section, the results of the uniaxial tensile test, provided in the form of force-displacement data, were converted to stress-strain data to define the mechanical properties of these structures. Mechanical properties such as Young's modulus, yield strength, and ultimate strength were extracted and used as input for the finite element software. The Abaqus/Explicit method was employed for simulating this test. To simulate the compression test, uniaxial displacement in the (Z) direction was defined for the upper plate. The lower plate, which rests on the fixed jaw of the machine, was completely constrained with all degrees of freedom restricted. The top plate, with displacement allowed in the (Z) direction, was set to a displacement of 25 mm. For meshing the samples, the Sweep method with a size of 0.15 was applied. This mesh size was obtained through mesh sensitivity study in exclude the effect of mesh size on the results. The boundary conditions were defined similarly, as shown in Figure 7. The results of this simulation were obtained in the form of force-displacement data, which were then used for comparison with the experimental results. General contact was implemented in the finite element simulations to account for

potential interactions between surfaces, including those not initially in contact, ensuring accurate modelling of deformation and collapse
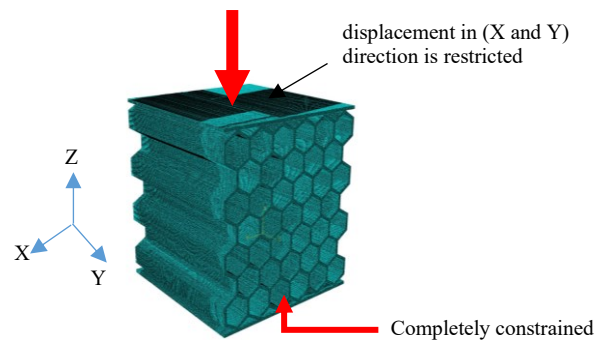

Fig.7 Sample of boundary conditions and meshed model

behaviour during compression. It worth noting that, he mechanical behavior of the 3D-printed PLA struts is inherently anisotropic due to the layer-by-layer nature of the FDM process. However, a balanced ±45° raster angle was employed to minimize in-plane anisotropy and promote quasi-isotropic behavior at the macro-scale. This approach is a well-established simplification in the literature for analyzing lattice structures, where the global performance is dominated by the architectural topology rather than the micro-scale material anisotropy of the individual struts [52]. The validity of this assumption is further supported by the strong correlation achieved between the experimental results and the numerical simulations that utilized an isotropic material model.

5- Result and Discussion

After conducting simulations for the samples and performing the compression test, in which two specimens were tested for each model and the average values were recorded, it is now time to compare them with each other and analyses the structures. In this section, the force-displacement diagram for each structure, obtained from experimental tests and FEA, is presented. The behavior of each structure, subjected to compressive loading, has been recorded step by step to examine the structural changes at various displacements. Subsequently, after completing this process for all four structures, the evaluation criteria EA, SEA, MCF and PCF are calculated and presented, and the optimal specimen is introduced.

5-1- Sample (1)

Figure 8 shows the force-displacement curve for Sample 1, that extracted from experimental tests and FEA. Figure 8 compares the experimental and FE force-displacement curves for Sample 1 under quasi-static compression.

The experimental curve exhibits the characteristic behavior of a cellular structure: an initial linear elastic rise, a peak force representing the onset of plastic yielding and cell wall buckling, followed by a progressive collapse plateau and a final sharp rise due to densification. The curve shows a peak crushing force (PCF) of approximately 3350 N and some minor fluctuations in the plateau region, indicative of the sequential buckling of individual cells and the inherent micro-imperfections from the 3D printing process.

The FE curve successfully captures the overall mechanical response, including the initial stiffness, the general trend of the collapse plateau, and the onset of densification. However, it predicts a lower PCF (approximately 2109 N) and a smoother plateau. This discrepancy is primarily due to the FE model's idealized geometry, which lacks the microscopic imperfections and slight geometric inaccuracies present in the physical prints that can trigger earlier failure.

Despite variations in the absolute peak force, the strong agreement in the overall force-displacement response and, crucially, in the total energy absorption (EA) validates the finite element (FE) model's capacity to reliably predict key crushing performance metrics for comparative analysis of the lattice designs. A qualitative comparison of experimental and FEA deformation modes at progressive displacement intervals is provided in Figure 9. Figure 9a (δ=0 mm) shows the initial state. Upon loading, cell walls initially undergo elastic bending, resulting in a linear deformation regime observed up to approximately δ=2.5 mm (Figure 9b). Beyond this yield point, progressive cell collapse signifies the onset of plastic deformation and sustained energy absorption. A cell is considered fully collapsed once its opposing walls contact under load (δ=18 mm, Figure 9c), at which point its energy absorption capacity is exhausted. Subsequent loading compacts the collapsed cells, leading to a rapid increase in structural stiffness and contact force, as the material densifies without significant further energy absorption (δ=19.5 mm, Figure 9d).
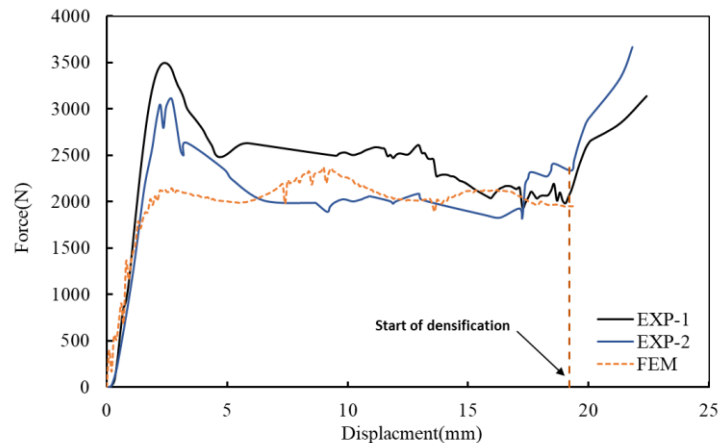

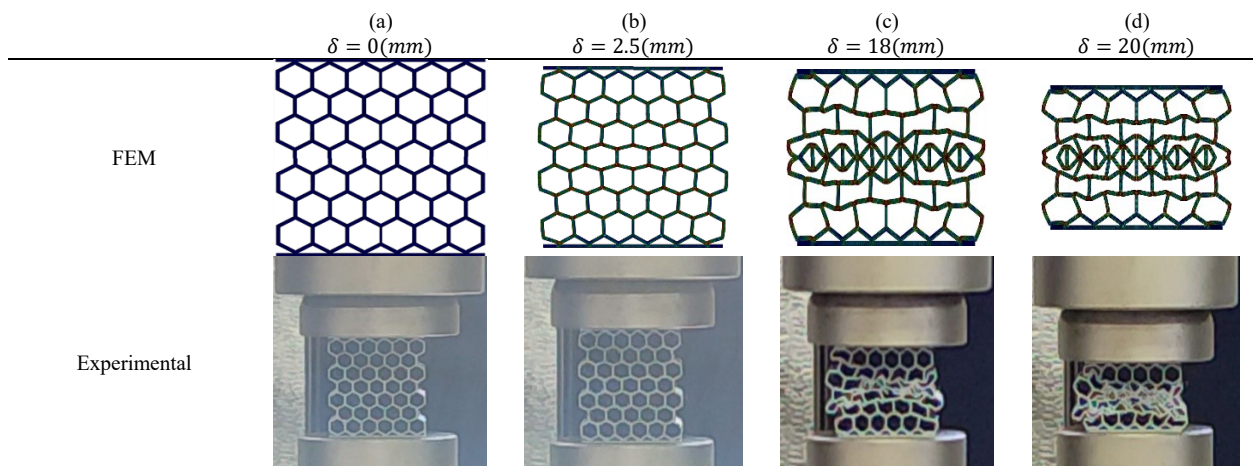**Fig.8** Force-Displacement curve for Experimental and FEM results

Fig.9 Comparison of experimental and FEM results at various displacement rates

5-2- Sample (2)

Figure 10 shows the force-displacement curve for Sample 2, that extracted from experimental tests and FEA. The experimental curve shows an initial peak followed by a fluctuating plateau and a sharp rise at densification. In this sample PCF value increased to 5810N. Comparing Figures 8 and 10 shows that re-entrant structure exhibits a significantly higher initial peak force and greater fluctuations during the progressive crushing phase. Additionally, Figure 11 illustrates the comparison of experimental results with FEA at various displacement values. Figure 11-(a) represents the initial state where displacement is zero (δ=0 mm). At the start of the process, the cell walls first bend, which leads to elastic deformation., which is linear and observed up to approximately (δ=2.5 mm) in this sample (Figure 11-(b)). Beyond this point, the displacement reaches a level where the cells begin to collapse, indicating a clear plastic deformation. During these phases, the structure absorbs energy, which continues as long as the cells have not fully collapsed. When the opposing walls of a single cell come into contact due to pressure, it can be said that the cell has been destroyed, and EA ceases (δ=17 mm) (Figure 11-(c)). After most cells have been destroyed, if force continues to be applied, the damaged cells compress against each other, causing the stiffness of the structure to increase. This allows it to withstand significant force, and from this point onward, the force increases noticeably (δ = 20mm) (Figure 11-(d)). At this stage, the structure becomes denser, and as mentioned earlier, no further EA occurs.
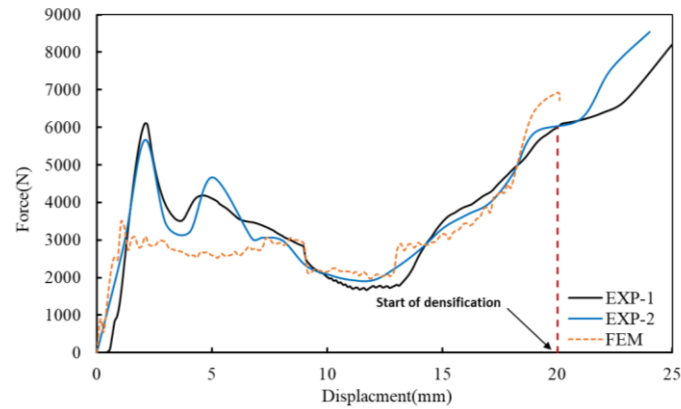
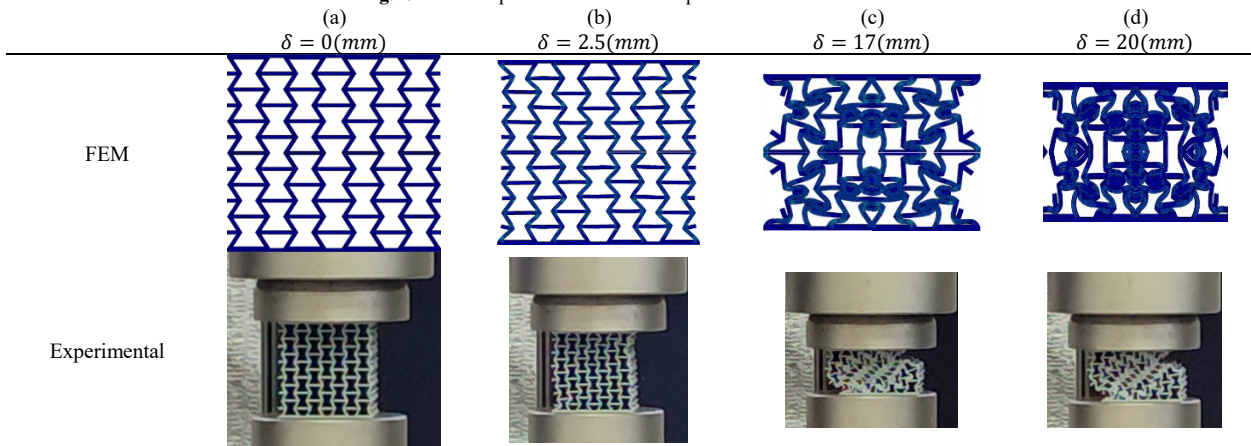**Fig.10** Force-Displacement curve for Experimental and FEM results

	(a) $\delta = 0(mm)$	(b) $\delta = 2.5(mm)$	(c) $\delta = 17(mm)$	(d) $\delta = 20(mm)$
FEM				
Experimental				

Fig.11 Comparison of experimental and FEM results at various displacement rates

5-3- Sample (3)

Figure12 shows the force-displacement curve for Sample 3 (hybrid structure), which exhibits a substantially higher peak crushing force and greater EA compared to both the honeycomb (Figure 8) and re-entrant (Figure10) samples. In this sample PCF value increased to 6882 N. Its collapse plateau is also more stable and sustained than the fluctuating plateau of the re-entrant structure. Additionally, Figure 13 illustrates the comparison of experimental results with FEA at various displacement rates. Figure 13-(a) represents the initial state where displacement is zero (δ=0 mm). At the start of the process, the cell walls first bend, which leads to elastic deformation., which is linear and observed up to approximately (δ=4 mm) in this sample (Figure 13-(b)). Beyond this point, the displacement reaches

a level where the cells begin to collapse, indicating a clear plastic deformation. During these phases, the structure absorbs energy, which continues as long as the cells have not fully collapsed. When the opposing walls of a single cell come into contact due to pressure, it can be said that the cell has been destroyed, and EA ceases (δ=16 mm) (Figure 13-(c)). After most cells have been destroyed, if force continues to be applied, the damaged cells compress against each other, causing the stiffness of the structure to increase. This allows it to withstand significant force, and from this point onward, the force increases noticeably (δ = 20mm) (Figure 13-(d)). At this stage, the structure becomes denser, and as mentioned earlier, no further EA occurs.
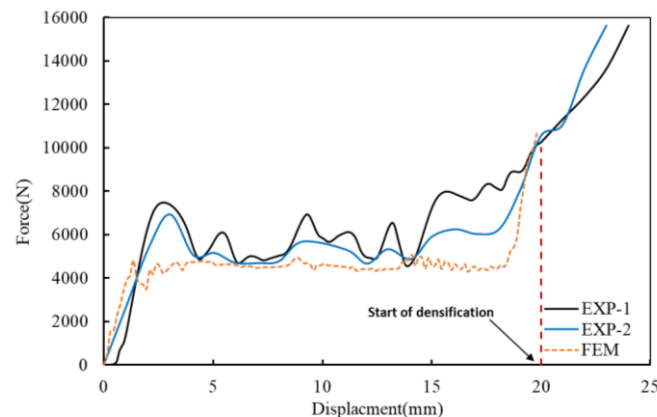

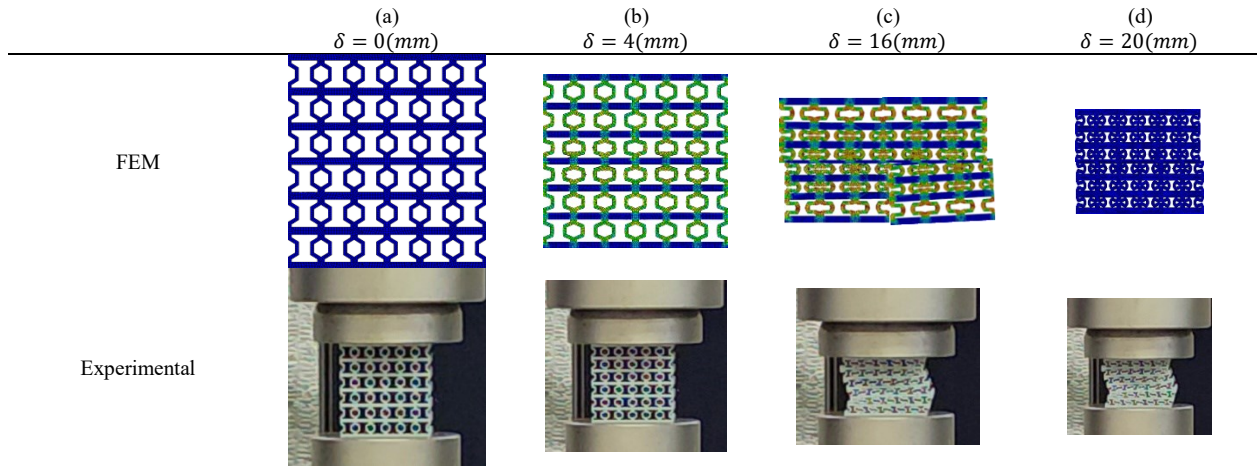**Fig.12** Force-Displacement curve for Experimental and FEM results.

	(a) $\delta = 0(mm)$	(b) $\delta = 4(mm)$	(c) $\delta = 16(mm)$	(d) $\delta = 20(mm)$
FEM				
Experimental				

Fig.13 Comparison of experimental and FEM results at various displacement rates

5-4- Sample (4)

Figure 14 presents the force-displacement curve for Sample 4, which achieves the highest and most stable plateau force of all, significantly outperforming the uniform honeycomb (Figure 8) and re-entrant (Figure 10) structures in both load-bearing consistency and overall EA capacity. In this sample PCF value increased to 7073.37N. Additionally, Figure 15 illustrates the comparison of experimental results with FEA at various displacement rates. Figure 15-(a) represents the initial state where displacement is zero (δ=0 mm). At the start of the process, the cell walls first bend, which leads to elastic deformation., which is linear and observed up to approximately (δ=3 mm) in this sample (Figure 15-(b)). Beyond this

point, the displacement reaches a level where the cells begin to collapse, indicating a clear plastic deformation. During these phases, the structure absorbs energy, which continues as long as the cells have not fully collapsed. When the opposing walls of a single cell come into contact due to pressure, it can be said that the cell has been destroyed, and EA ceases (δ=18 mm) (Figure 15-(c)). After most cells have been destroyed, if force continues to be applied, the damaged cells compress against each other, causing the stiffness of the structure to increase. This allows it to withstand significant force, and from this point onward, the force increases noticeably (δ = 19mm) (Figure 15-(d)). At this stage, the structure becomes denser, and as mentioned earlier, no further EA occurs.
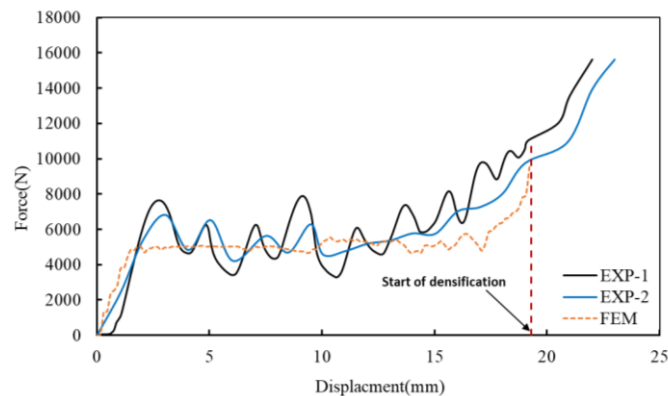
Fig.14 Force-Displacement curve for Experimental and FEM results

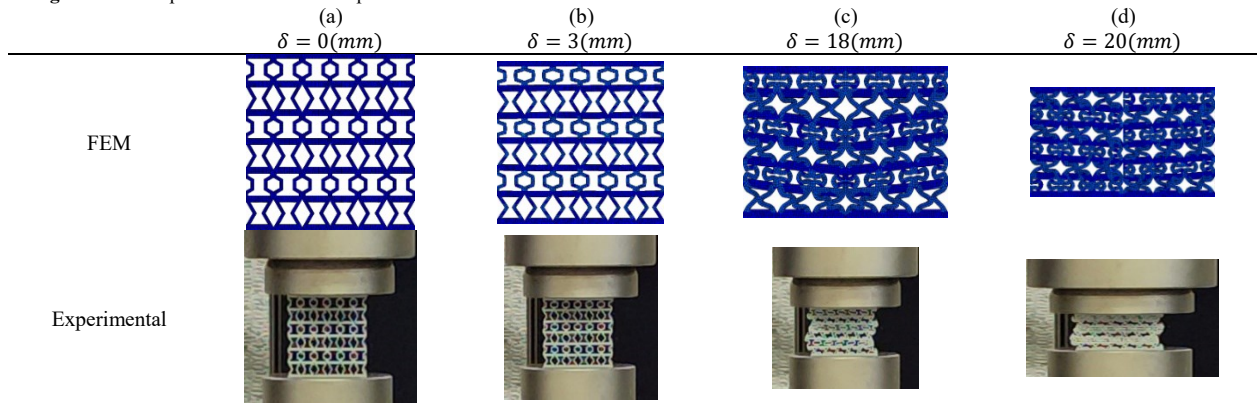|	(a) $\delta = 0(mm)$	(b) $\delta = 3(mm)$	(c) $\delta = 18(mm)$	(d) $\delta = 20(mm)$
FEM				
Experimental				

Fig.15 Comparison of experimental and FEM results at various displacement rates

Now, to evaluate the performance of these four samples, they need to be calculated based on the introduced criteria. One of the most important factors that distinguishes between lattice structures is

their EA capacity. Figure 16, compares the EA for all four samples, showing both the average experimental values and the corresponding FE simulation results. It visually demonstrates that

Sample 4 absorbed the most total energy, followed by Sample 3, with the uniform structures (Samples 1 and 2) absorbing the least. Figure 17 compares the SEA, which normalizes the EA by the mass of the structure. This figure highlights that the hybrid designs (Samples 3 and 4) are the most efficient, with Sample 4 achieving the highest SEA, confirming that its superior performance is not due to simply being heavier but to a more effective geometric design. Figure 18 shows the MCF values which represents the average force sustained throughout the crushing displacement. It shows that Samples 3 and 4 sustained a much higher average load than Samples 1 and 2, with Sample 4 having the highest MCF, indicating its superior and more consistent load-bearing capability during collapse. Figure 19 compares the experimental and simulated PCF values, a critical parameter calculated to assess the initial structural strength and the maximum load the absorber must withstand before collapsing. This figure shows that sample 3 and 4 exhibits highest PCF value. Table 3 shows the values for EA, SEA, MCF, CFE for each sample in the experimental test and FEM. Overall, in sample 1, there was a 14.08% difference between the experimental and FEM results across all indices; in sample 2, this difference was 9.36%; in sample 3, it was 16.67%; and in sample

4, it was 15.16%. Despite these differences, there is an acceptable level of agreement between the experimental and FEM results. However, the observed discrepancy in the values between the experimental and FEM results can be partially attributed to the fact that the numerical model utilized a rate-independent material law, thereby not capturing the slight strain-rate sensitivity of the PLA material under the quasi-static testing conditions. Beyond total energy absorption, the Crushing Force Efficiency (CFE) is a critical metric that evaluates the stability and consistency of the crushing force. A higher CFE indicates a more stable collapse with a lower initial peak force relative to the mean force, which is highly desirable for predictable and efficient energy absorption. As shown in Table 3, the hybrid structures (Samples 3 and 4) demonstrated superior CFE values of 87.1% and 87.3%, respectively. This represents a significant improvement over the uniform auxetic structure (Sample 2, 59.1%) and the conventional honeycomb (Sample 1, 70.2%), confirming that the hybrid designs not only absorb more energy but also do so in a much more stable and efficient manner.
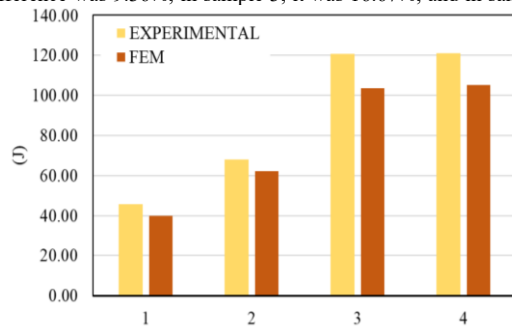

Fig.16 Comparison Plot of average experimental values of EA versus FE values
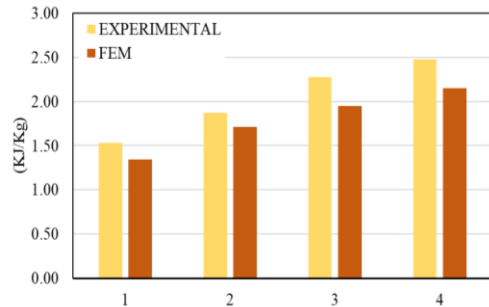

Fig.18 Comparison Plot of average experimental values of MCF versus FE values

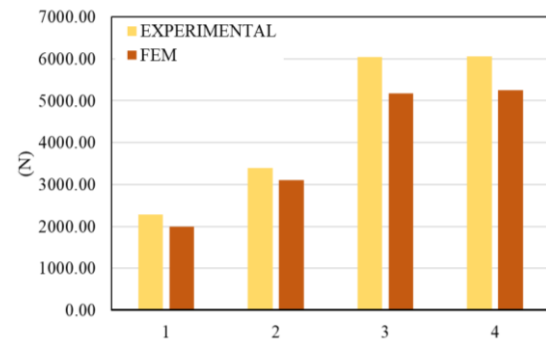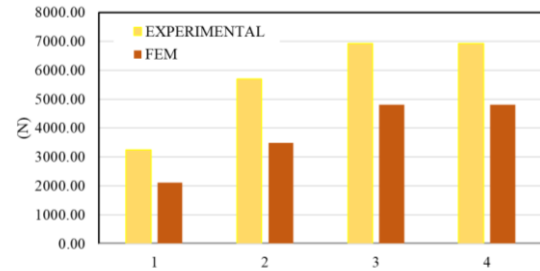**Fig.17** Comparison Plot of average experimental values of SEA versus FE values

Fig.19 Comparison Plot of average experimental values of PCF versus FE values

Table.3 Values of EA, SEA, MCF, PCF and CFE for samples

Evaluation Criteria	Type of test	Sample (1)	Sample (2)	Sample (3)	Sample (4)
EA(J)	Experimental	45.64	68.00	120.75	121.05
		44.36	65.95	118.25	119.98
	FEM	40.00	62.18	103.50	105.11
SEA(KJ/Kg)	Experimental	1.53	1.87	2.27	2.48
		1.49	1.44	2.21	2.34
	FEM	1.34	1.71	1.95	2.15
MCF(N)	Experimental	2281.82	3400.14	6037.45	6052.36
		2165.97	3346.32	5901.12	5913.56
	FEM	2000.13	3109.22	5174.90	5255.43
PCF	Experimental	3450.00	5980.00	6932.00	7223.12
		3250.00	5700.00	6832.10	6923.62
	FEM	2109.12	3485.12	4815.23	4801.12
CFE (%)	Experimental	70.2	59.1	87.1	87.3

6- Conclusion

This study investigated the energy absorption (EA) performance of four 3D-printed lattice structures under quasi-static compression, focusing on the effects of combining auxetic and conventional cell geometries. Through experimental testing and finite element simulations, several key findings emerged:

1. Hybrid designs outperformed uniform structures. Sample 4 (a combination of auxetic and honeycomb cells) achieved the highest specific energy absorption (SEA) of 2.48 kJ/kg—a 38% increase over the conventional honeycomb (Sample 1).

2. Geometric hybridization proved more effective for enhancing EA than material modification. This was demonstrated by the superior performance of monolithic polylactic acid (PLA) hybrid structures compared to the multi-material designs reported in the literature.

3. Finite element analysis (FEA) using a general contact algorithm successfully captured the complex deformation mechanisms, showing strong agreement with experimental results.

These findings highlight that strategic cell combination, rather than increased material complexity, can significantly improve energy absorption in lightweight structures. The results provide practical insights for applications requiring impact protection, such as aerospace components, automotive crumple zones, and personal protective equipment. Future work could explore dynamic loading conditions and the optimization of hybrid cell topologies for targeted performance metrics.

Ethics Approval:

The scientific content of this article is the result of the authors' research and has not been published in any Iranian or international journal.

Conflict of Interest:

The authors declare that they have no conflicts of interest to this work.

References

[1] Paygozar, B. and M.S. Sadigh, A new hybrid energy absorption mechanism subjected to axial loading. Journal of Central South University, 2020. 27(1): p. 76-87. https://doi.org/10.1007/s11771-020-4279-0.

[2] Paygozar, B. and M.S. Sadigh, Practicability of metallic hybrid systems in enhancing the energy absorption capacity: expansion and buckling mechanisms. Journal of the Brazilian Society of Mechanical Sciences and Engineering, 2020. 42(6): p. 307. https://doi.org/10.1007/s40430-020-02405-3.

[3] A. Ghaedizadeh, J. Shen, X. Ren, and Y. M. Xie, "Tuning the performance of metallic auxetic metamaterials by using buckling and plasticity," Materials, vol. 9, no. 1, p. 54, 2016.

[4] R. Critchley, I. Corni, J. A. Wharton, F. C. Walsh, R. J. Wood, and K. R. Stokes, "A review of the manufacture, mechanical properties and potential applications of auxetic foams," physica status solidi (b), vol. 250, no. 10, pp. 1963-1982, 2013, doi: https://doi.org/10.1002/pssb.201248550.

[5] J. Shen, S. Zhou, X. Huang, and Y. M. Xie, "Simple cubic three‐dimensional auxetic metamaterials," physica status solidi (b), vol. 251, no. 8, pp. 1515-1522, 2014, doi: https://doi.org/10.1002/pssb.201451304.

[6] X. Ren, R. Das, P. Tran, T. D. Ngo, and Y. M. Xie, "Auxetic metamaterials and structures: a review," Smart materials and structures, vol. 27, no. 2, p. 023001, 2018, doi: https://doi.org/10.1088/1361-665X/aaa61c.

[7] X. Y. Zhang and X. Ren, "A simple methodology to generate metamaterials and structures with negative Poisson's ratio," physica status solidi (b), vol. 257, no. 10, p. 2000439, 2020, doi: https://doi.org/10.1002/pssb.202000439.

[8] N. Novak, M. Vesenjak, and Z. Ren, "Auxetic cellular materials-a review," Strojniški vestnik-Journal of Mechanical Engineering, vol. 62, no. 9, pp. 485-493, 2016, doi: https://doi.org/10.5545/sv-jme.2016.3656.

[9] C. Luo, C. Z. Han, X. Y. Zhang, X. G. Zhang, X. Ren, and Y. M. Xie, "Design, manufacturing and applications of auxetic tubular structures: A review," Thin-Walled Structures, vol. 163, p. 107682, 2021, doi: https://doi.org/10.1016/j.tws.2021.107682.

[10] R. Lakes and K. Elms, "Indentability of conventional and negative Poisson's ratio foams," Journal of Composite Materials, vol. 27, no. 12, pp. 1193-1202, 1993, doi: https://doi.org/10.1177/002199839302701203.

[11] V. H. Carneiro, J. Meireles, and H. Puga, "Auxetic materials— A review," Materials Science-Poland, vol. 31, pp. 561-571, 2013, doi: https://doi.org/10.2478/s13536-013-0140-6.

[12] Adibeig, M.R., et al., Quasi-static simulation and fatigue life estimation of fused filament fabrication of polylactic acid specimens using finite element method. Journal of Manufacturing Processes, 2023. 106: p. 202-213., https://doi.org/10.1016/j.jmapro.2023.09.071.

[13] Adibeig, M.R., F. Vakili-Tahami, and M.-A. Saeimi-Sadigh, Numerical and experimental investigation on creep response of 3D printed Polylactic acid (PLA) samples. Part I: The effect of building direction and unidirectional raster orientation. Journal of the Mechanical Behavior of Biomedical Materials, 2023. 145: p. 106025. https://doi.org/10.1016/j.jmbbm.2023.106025

[14] G. Imbalzano, P. Tran, T. D. Ngo, and P. V. Lee, "A numerical study of auxetic composite panels under blast loadings," Composite Structures, vol. 135, pp. 339-352, 2016, doi: https://doi.org/10.1016/j.compstruct.2015.09.038.

[15] A. Alomarah, D. Ruan, S. Masood, and Z. Gao, "Compressive properties of a novel additively manufactured 3D auxetic structure," Smart Materials and Structures, vol. 28, no. 8, p. 085019, 2019, doi: https://doi.org/10.1088/1361-665X/ab0dd6.

[16] J. Simpson and Z. Kazancı, "Crushing investigation of crash boxes filled with honeycomb and re-entrant (auxetic) lattices," Thin-Walled Structures, vol. 150, p. 106676, 2020, doi: https://doi.org/10.1016/j.tws.2020.106676.

[17] G. Imbalzano, S. Linforth, T. D. Ngo, P. V. S. Lee, and P. Tran, "Blast resistance of auxetic and honeycomb sandwich panels: Comparisons and parametric designs," Composite Structures, vol. 183, pp. 242-261, 2018, doi: https://doi.org/10.1016/j.compstruct.2017.03.018.

[18] S. Xie, Z. Feng, H. Zhou, and D. Wang, "Three-point bending behavior of Nomex honeycomb sandwich panels: Experiment and simulation," Mechanics of Advanced Materials and Structures, vol. 28, no. 18, pp. 1917-1931, 2021, doi: https://doi.org/10.1080/15376494.2020.1712751.

[19] H. Taghipoor, A. Eyvazian, F. Musharavati, T. Sebaey, and A. Ghiaskar, "Experimental investigation of the three-point bending properties of sandwich beams with polyurethane foam-filled lattice cores," in Structures, 2020, vol. 28: Elsevier, pp. 424-432, doi: https://doi.org/10.1016/j.istruc.2020.08.082.

[20] J. Xiang and J. Du, "Energy absorption characteristics of bio-inspired honeycomb structure under axial impact loading," Materials Science and Engineering: A, vol. 696, pp. 283-289, 2017, doi: https://doi.org/10.1016/j.msea.2017.04.044.

[21] H. Tan, Z. He, K. Li, E. Li, A. Cheng, and B. Xu, "In-plane crashworthiness of re-entrant hierarchical honeycombs with negative Poisson's ratio," Composite Structures, vol. 229, p. 111415, 2019, doi: https://doi.org/10.1016/j.compstruct.2019.111415.

[22] F. Sun, C. Lai, and H. Fan, "In-plane compression behavior and energy absorption of hierarchical triangular lattice structures," Materials & Design, vol. 100, pp. 280-290, 2016, doi: https://doi.org/10.1016/j.matdes.2016.03.023.

[23] D. Zhang, Q. Fei, J. Liu, D. Jiang, and Y. Li, "Crushing of vertex-based hierarchical honeycombs with triangular substructures," Thin-Walled Structures, vol. 146, p. 106436, 2020, doi: https://doi.org/10.1016/j.tws.2019.106436.

[24] D. Xiao, X. Chen, Y. Li, W. Wu, and D. Fang, "The structure response of sandwich beams with metallic auxetic honeycomb cores under localized impulsive loading-experiments and finite element analysis," Materials & Design, vol. 176, p. 107840, 2019, doi: https://doi.org/10.1016/j.matdes.2019.107840.

[25] E. Pei, J. Shen, and J. Watling, "Direct 3D printing of polymers onto textiles: experimental studies and applications," Rapid Prototyping Journal, vol. 21, no. 5, pp. 556-571, 2015, doi: https://doi.org/10.1108/RPJ-09-2014-0126.

[26] M. Kowalska, M. Woźniak, M. Kijek, P. Mitrosz, J. Szakiel, and P. Turek, "Management of validation of HPLC method for determination of acetylsalicylic acid impurities in a new pharmaceutical product," Scientific Reports, vol. 12, no. 1, p. 1, 2022, doi: https://doi.org/10.1038/s41598-021-99269-x.

[27] H. Rahman, E. Yarali, A. Zolfagharian, A. Serjouei, and M. Bodaghi, "Energy absorption and mechanical performance of

functionally graded soft–hard lattice structures," Materials, vol. 14, no. 6, p. 1366, 2021, doi: https://doi.org/10.3390/ma14061366.

[28] D. Photiou, S. Avraam, F. Sillani, F. Verga, O. Jay, and L. Papadakis, "Experimental and numerical analysis of 3d printed polymer tetra-petal auxetic structures under compression," Applied Sciences, vol. 11, no. 21, p. 10362, 2021, doi: https://doi.org/10.3390/app112110362.

[29] M. S. Rad, H. Hatami, R. Alipouri, A. F. Nejad, and F. Omidinasab, "Determination of energy absorption in different cellular auxetic structures," Mechanics & Industry, vol. 20, no. 3, p. 302, 2019, doi: https://doi.org/10.1051/meca/2019019.

[30] A. Yousefi, S. Jolaiy, M. Lalegani Dezaki, A. Zolfagharian, A. Serjouei, and M. Bodaghi, "3D‐Printed soft and hard meta‐structures with supreme energy absorption and dissipation capacities in cyclic loading conditions," Advanced Engineering Materials, vol. 25, no. 4, p. 2201189, 2023, doi: https://doi.org/10.1002/adem.202201189.

[31] D. Li, J. Yin, L. Dong, and R. S. Lakes, "Strong re-entrant cellular structures with negative Poisson's ratio," Journal of materials science, vol. 53, no. 5, pp. 3493-3499, 2018, doi: https://doi.org/10.1007/s10853-017-1809-8.

[32] M.-H. Fu, Y. Chen, and L.-L. Hu, "Bilinear elastic characteristic of enhanced auxetic honeycombs," Composite Structures, vol. 175, pp. 101-110, 2017, doi: https://doi.org/10.1016/j.compstruct.2017.04.007.

[33] M.-H. Fu, Y. Chen, and L.-L. Hu, "A novel auxetic honeycomb with enhanced in-plane stiffness and buckling strength," Composite Structures, vol. 160, pp. 574-585, 2017, doi: https://doi.org/10.1016/j.compstruct.2016.10.090.

[34] X. Li, Z. Lu, Z. Yang, and C. Yang, "Directions dependence of the elastic properties of a 3D augmented re-entrant cellular structure," Materials & Design, vol. 134, pp. 151-162, 2017, doi: https://doi.org/10.1016/j.matdes.2017.08.024.

[35] M. Zahed, R. Ardeshiri Jouneghani, and M. Safarabadi, "Reinforcement of 3D‐printed re‐entrant structures using additional supports under three‐point bending, experimental and numerical analyses," Advanced Engineering Materials, vol. 26, no. 1, p. 2301252, 2024, doi: https://doi.org/10.1002/adem.202301252.

[36] H. Wang, Z. Lu, Z. Yang, and X. Li, "A novel re-entrant auxetic honeycomb with enhanced in-plane impact resistance," Composite Structures, vol. 208, pp. 758-770, 2019, doi: https://doi.org/10.1016/j.compstruct.2018.10.024.

[37] M. S. Ebrahimi, R. Hashemi, and E. Etemadi, "In-plane energy absorption characteristics and mechanical properties of 3D printed novel hybrid cellular structures," journal of materials research and technology, vol. 20, pp. 3616-3632, 2022, doi: https://doi.org/10.1016/j.jmrt.2022.08.064.

[38] A. Alomarah, S. H. Masood, I. Sbarski, B. Faisal, Z. Gao, and D. Ruan, "Compressive properties of 3D printed auxetic structures: experimental and numerical studies," Virtual and Physical Prototyping, vol. 15, no. 1, pp. 1-21, 2020, doi: https://doi.org/10.1080/17452759.2019.1644184.

[39] R. Johnston and Z. Kazancı, "Analysis of additively manufactured (3D printed) dual-material auxetic structures under compression," Additive Manufacturing, vol. 38, p. 101783, 2021, doi: https://doi.org/10.1016/j.addma.2020.101783.

[40] S. Yuan, C. K. Chua, and K. Zhou, "3D‐printed mechanical metamaterials with high energy absorption," Advanced Materials

Technologies, vol. 4, no. 3, p. 1800419, 2019, doi: https://doi.org/10.1002/admt.201800419.

[41] J. Wu, Y. Zhang, F. Zhang, Y. Hou, and X. Yan, "A bionic tree-liked fractal structure as energy absorber under axial loading," Engineering Structures, vol. 245, p. 112914, 2021, doi: https://doi.org/10.1016/j.engstruct.2021.112914.

[42] M. Najafi, H. Ahmadi, and G. Liaghat, "Experimental investigation on energy absorption of auxetic structures," Materials today: proceedings, vol. 34, pp. 350-355, 2021, doi: https://doi.org/10.1016/j.matpr.2020.06.075.

[43] T. Tancogne-Dejean, A. B. Spierings, and D. Mohr, "Additively-manufactured metallic micro-lattice materials for high specific energy absorption under static and dynamic loading," Acta Materialia, vol. 116, pp. 14-28, 2016, doi: https://doi.org/10.1016/j.actamat.2016.05.054.

[44] N. Sui, X. Yan, T.-Y. Huang, J. Xu, F.-G. Yuan, and Y. Jing, "A lightweight yet sound-proof honeycomb acoustic metamaterial," Applied Physics Letters, vol. 106, no. 17, 2015, doi: https://doi.org/10.1063/1.4919235.

[45] S. J. Yeo, M. J. Oh, and P. J. Yoo, "Structurally controlled cellular architectures for high‐performance ultra‐lightweight materials," Advanced Materials, vol. 31, no. 34, p. 1803670, 2019, doi: https://doi.org/10.1002/adma.201803670.

[46] N. K. Choudhry, B. Panda, and U. S. Dixit, "Energy absorption characteristics of fused deposition modeling 3D printed auxetic re-entrant structures: a review," Journal of Materials Engineering and Performance, vol. 32, no. 20, pp. 8981-8999, 2023, doi: https://doi.org/10.1007/s11665-023-08243-3.

[47] H. Y. Sarvestani, A. Akbarzadeh, H. Niknam, and K. Hermenean, "3D printed architected polymeric sandwich panels: Energy absorption and structural performance," Composite Structures, vol. 200, pp. 886-909, 2018, doi: https://doi.org/10.1016/j.compstruct.2018.04.002.

[48] N. Namvar, A. Zolfagharian, F. Vakili-Tahami, and M. Bodaghi, "Reversible energy absorption of elasto-plastic auxetic, hexagonal, and AuxHex structures fabricated by FDM 4D printing," Smart Materials and Structures, vol. 31, no. 5, p. 055021, 2022, doi: https://doi.org/10.1088/1361-665X/ac6291.

[49] R. Sarkhosh, "Enhanced Specific Energy Absorption in Honeycomb Structures with Novel Spiral Reinforcement and Foam Filling," *Polymer Engineering & Science,* 2025, doi: https://doi.org/10.1002/pen.27294.

[50] R. Sarkhosh, "Enhanced crashworthiness and energy absorption properties of honeycomb structures with a novel sunflower-inspired design," *Journal of the Brazilian Society of Mechanical Sciences and Engineering,* vol. 47, no. 7, p. 322, 2025, doi: https://doi.org/10.1007/s40430-025-05634-6.

[51] R. Sarkhosh, A. Farrokhabadi, and H. Zarei, "Crashworthiness characteristics of composite cylindrical energy absorbers filled with honeycomb and foam under quasi-static loading," *J. Braz. Soc. Mech. Sci. Eng.*, vol. 44, no. 8, p. 346, 2022, doi: https://doi.org/10.1007/s40430-022-03651-3.

[52] Ebrahimi, M.S., R. Hashemi, and E. Etemadi, In-plane energy absorption characteristics and mechanical properties of 3D printed novel hybrid cellular structures. journal of materials research and technology, 2022. 20: p. 3616-3632.